IIETA International Information and Engineering Technology Association
Advancing the World of Information and Engineering

Traitement du Signal
Vol. 41, No. 5, October, 2024, pp. 2339-2353
Journal homepage: http://iieta.org/journals/ts

A Novel Approach for Glaucoma Classification by Wavelet Neural Networks Using Statistical and Graph-Based Features of Qualitatively Improved Images

Krishna Santosh Naidana*, Soubhagya Sankar Barpanda

School of Computer Science and Engineering, VIT-AP University, Amaravati 522237, India

Corresponding Author Email: krishna.18phd7018@vitap.ac.in

https://doi.org/10.18280/ts.410510

Received: 14 August 2023
Revised: 22 March 2024
Accepted: 12 July 2024
Available online: 31 October 2024

Keywords:
glaucoma, image improvement, local graph structures, graph shortest paths, wavelet neural networks

ABSTRACT

In this paper, we have proposed a new glaucoma classification approach that employs a wavelet neural network (WNN) on optimally enhanced retinal images' features. To avoid tedious and error-prone manual analysis of retinal images, computer-aided diagnosis (CAD) substantially aids in robust diagnosis. Our proposal has a significant contribution to make in all major CAD phases. Retinal image quality improvement is attempted in two phases. The retinal image preprocessing phase improves the brightness and contrast of the image through quantile-based histogram modification. It is followed by the image structural enhancement phase, which involves multi-scale morphological operations using image-specific dynamic structuring elements (SE). Graph-based retinal image features in terms of Local Graph Structures (LGS) and Graph Shortest Path (GSP) statistics are extracted from various directions along with the statistical features from the enhanced images. WNN is employed to classify glaucoma retinal images with a suitable wavelet activation function. The performance of the WNN classifier is compared with that of multilayer perceptron neural networks (MLP) and the state-of-the art approaches to prove its efficacy.

1. INTRODUCTION

In human life, vision plays a critical role in coordinating daily activities. There are harmful diseases that can affect vision more than the adverse effects caused by accidents. The primary cause [1] of vision disability is glaucoma development. There are a variety of approaches to detecting glaucoma in the early stages [2], most of which are based on medical examination through the fundus (retinal) image structures [3]. Manually inspecting retinal images, on the other hand, is a tedious task. In this case, CAD [4] has proven to be a valuable tool for ophthalmologists in interpreting the eye fundus images for a rapid and accurate glaucoma screening. The major phases of CAD are image improvement, feature extraction, and classification. Several existing CAD approaches exhibit potential in screening glaucoma from various medical imaging modalities such as fundus photography. However, they come with certain limitations. The current approaches use large retinal image datasets to demonstrate their effectiveness, but acquiring these datasets is challenging and time-consuming. Another significant limitation is class imbalance, where the number of healthy samples greatly exceeds or falls short of the number of glaucomatous samples. This can bias the model toward the majority class and diminish its ability to accurately classify the minority class. Present convolutional-based glaucoma screening approaches are often criticized for their lack of interpretability since originally they are trained on non-medical images. In medical contexts, understanding the rationale behind a model's classification decisions is essential due to the significant consequences of these decisions. Lack of model generalization is another issue in the retinal image pattern recognition. Retinal images frequently lack quality and standardization due to factors like low contrast, uneven illumination, and imaging conditions. While current CAD approaches focus primarily on identifying retinal image patterns, there's a need to address image enhancement. Improving visualization of retinal structures and abnormalities can facilitate clinicians in detecting subtle disease signs. Techniques that enhance features like blood vessels, the optic disc (OD), and the macula can aid in early glaucoma detection and accurate diagnosis.

To overcome these challenges, a CAD-based glaucoma screening approach is needed, one that prioritizes interpretability and generalization, even when faced with limited training data and potential class imbalance issues. Such an approach should place equal emphasis on retinal image improvement and pattern identification. Thus, in this paper, we have proposed a novel CAD system whose significant contributions are utilizing quantile-based preprocessing for mapping image histograms and complex wavelet-based image enhancement using dynamic SE. It is followed by a robust feature extraction phase that considers both statistical and graph-based features, which are employed for retinal image classification using WNN and MLP.

The rest of the paper is organized into different portions: Section 2 reviews the related work; Section 3 illustrates the proposed CAD-based approach for glaucoma diagnosis; Section 4 analyzes the results for performance appraisal, and Section 5 concludes the paper.

2. RELATED WORK

In the proposed method, our contribution exists in retinal image enhancement, novel feature extraction, and classification. So far, numerous practices have been proposed in all these CAD phases. Out of all the contributions, some significant contributions are discussed below.

It is essential to improve the visual quality of retinal image structures for effective feature extraction. Gupta and Tiwari [5], Kim [6], and Sim et al. [7] employ adaptive gamma correction (AGC) and histogram equalization (HE) approaches to enhance the luminosity of the image without the occurrence of a gamut problem. Histogram modification based on recursive procedures and optimization is given by Wang et al. [8] and Arici et al. [9], but these approaches are not optimal due to their recursive nature. Thresholding is applied by Khare [10] to correct the non-illumination regions before enhancing contrast using the HE approach. Luo et al. [11] applied non-linear transformations to images to improve their contrast before noise suppression. A discrete wavelet transformation (DWT) is applied by Mallat [12]. DWT limitations are addressed by Selesnick et al. [13] by proposing a complex wavelet transformation (CWT)-based image enhancement. The contourlet transform (CT) of the image was proposed by Feng et al. [14], using non-linear functions. Images are sharpened and smoothed by Sujitha et al. [15] before denoising them. Liao et al. [16] applied a top-hat transformation (TH) with multi-scale to improve the image based on brighter and dim regions.

The proposed approach mainly concentrated on statistical and graph-based features of the retinal image. The co-occurrence matrix of image gray level (GLCM) was used by Tabbakh et al. [17] to extract the second-order features. Wavelet features are extracted from the image by Dua et al. [18] to classify images using Naïve Bayes (NB) [19], Support Vector Machine (SVM) [20], and Random Forest (RM) [21] approaches. Ranked cross-entropy image features are utilized by Shubhangi and Parveen [22]. Statistical image features are employed by Septiarini et al. [23] for higher accuracy. Local binary pattern (LBP)-based features are extracted by de Sousa et al. [24] for glaucoma classification. Singh et al. [25] extracted DWT features from the vessel's free optic disc area to get higher accuracy in ANN [26] classification. A hybrid feature set is formed with structural and non-structural features by Salam et al. [27]. Images' higher-order spectra (HOS) features are optimized by linear discriminant analysis (LDA) prior to applying SVM and NB classifiers by Noronha et al. [28] and Acharya et al. [29]. Image texture features can also be extracted from the equivalent graphs obtained from fundus images, which come under graph-based features. Abusham et al. [30] formed a binary relationship pattern for texture features using the graph formed by image mapping. Junior et al. [31] extracted the shortest paths from the image equivalent graph to generate texture features for image categorization. The nearest neighbor classifier (k-NN) is employed by Li et al. [32] on statistical retinal image features for higher accuracy.

It has been observed from the existing literature that prior to feature extraction, image quality improvement is carried out either by focusing on image brightness and contrast or on image structures, but not both. Regarding feature extraction, there is no specific approach to capturing the image texture pattern. This motivated us to propose a novel approach for the image quality enhancement, feature extraction, and classification phases of CAD-based glaucoma detection. Concerning retinal image quality, both colour adjustment and retinal structural improvement are necessary. Thus, we have incorporated two sub-phases into retinal image quality improvement to achieve intensity adjustment and structural improvement. The CAD approach to image classification is heavily based on the patterns of image textures. This led us to identify a new approach called graph-based image feature extraction, along with statistical features for glaucoma classification. We have introduced WNN for glaucoma screening. Our proposed approach employs WNN for the first time in glaucoma classification, based on existing literature.

3. THE PROPOSED CAD-BASED GLAUCOMA DIAGNOSIS

The proposed CAD approach is carried out on various public datasets [33] such as:

ACRIMA: This dataset has been created with a pixel resolution 2048×1536 as a part of the ACRIMA project by CVB labs, Spain. These retinal images are captured from the selected patients with a 35° Field of View (FOV) with a Topcon TRC fundus camera and labelled by Fisabio Medical Ophthalmology experts. This dataset contains a total of 705 fundus images, of which 309 are healthy images and 396 are glaucomatous retinal images.

ORIGA: This dataset is an online repository that contains 650 labelled retinal images with 482 healthy and 168 glaucomatous cases. These retinal images were captured from the Singapore Malay Eye Study by the eye research institute (SiMES) in a multi-environment framework that supports image segmentation, grading, and classification. Image grading follows the Centre for Eye Research Australia's protocol.

DRISHTI: This dataset has been published by the Centre for visual information technology, IIIT-Hyderabad in collaboration with Arvind eye hospital, Madhurai, India. It contains 101 fundus images out of which 31 are healthy images and 70 are glaucomatous images. Images are acquired from the dilated eyes of above 40 years age patients with a FOV of 30°, OD cantered with 2896×1944 resolutions. The primary objective of this dataset is to segment optic nerve head, i.e. OD of retinal images.

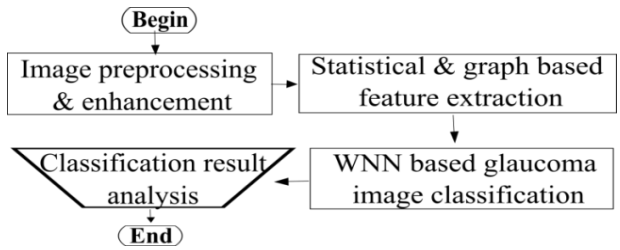

Figure 1. High level process flow of the proposed method

The overall flow of the proposed method of CAD glaucoma diagnosis is shown in Figure 1. The proposed process begins with retinal image preprocessing followed by enhancement for the visual improvement of images. Each image feature vector is fed to WNN and MLP classifiers to diagnose the image type (normal or abnormal). Classifier findings are analyzed to draw significant conclusions. This section explains the proposed image preprocessing, enhancement, and feature extraction w.r.t corresponding algorithm steps (*An:Sn*).

3.1 Retinal image pre-processing

The proposed preprocessing qualitatively improves the retinal image by systematically increasing brightness and contrast, as given in the *Algorithm: A1*. It begins by making the image's gray intensity (*GI*) histogram ($HIST_{GI}$) closer to the uniform histogram ($HIST_U$) (*A1:S2*) using an optimal proportion value α_{opt}. We have experimented with various values for α_{opt} and qualitative results are obtained for $0.3 \le \alpha_{opt} \le 0.7$ with no over improvement. Using the resultant mapped histogram (*Mh*), a normalized CDF (F_{CDF}) is generated. Instead of conventional F_{CDF} usage, a Quadratic Rank Transmutation Map (QRTM) [34] transformation of CDF (CDF_T) has been applied to provide a skew-kurtotic normal distribution (*A1:S4*). In this transformation, range of δ is [-1, 1]. Then, modified adaptive gamma correction (AGC) [35] is carried out to form a brighter image (I_{AGC}) (*A5:S5*) using image's maximum intensity I_{max}. During this process, image color information may slightly fluctuate, which can be restored by the input retinal image (I_{ORG}) color information (*A1:S6*). The resultant IMG_{pre} is a luminous and brightness enhanced image. It is then subjected to contrast improvement using a quantile-based approach. In terms of image intensities, quantiles are intensity values generated using the probability distribution function (PDF) of the image histogram (H_{pre}) over maximum and minimum intensities [I_{min}, I_{max}]. In this approach, *t-quantiles* are generated for IMG_{pre} by histogram splitting, as $H_{pre1} = [i_0, i_1]$, $H_{pre2} = [i_1, i_2], \ldots, H_{pre\text{-}t} = [i_{t\text{-}1}, i_t]$ and the corresponding normalized $CDF_{pre\text{-}k}$ for each sub-histogram is generated. The final pre-processed image (IMG_{PRE}) is obtained using sub-histogram mapping (*A1:S7*). The resultant pre-processed images are enriched with sufficient brightness and contrast. These pre-processed images are fed into the image enhancement.

3.2 Retinal image enhancement

The proposed enhancement technique aims to increase the quality of retinal image structures as described in *Algorithm: A2*. Dual tree CWT (DT-CWT) high and low-pass sub-bands (SB) [36, 37] are obtained from IMG_{PRE}. After this, the low and high pass SB coefficients (*C*) are processed independently as described in the following sub-sections.

3.2.1 Low-pass coefficient enhancement using dynamic SE-based morphological operation

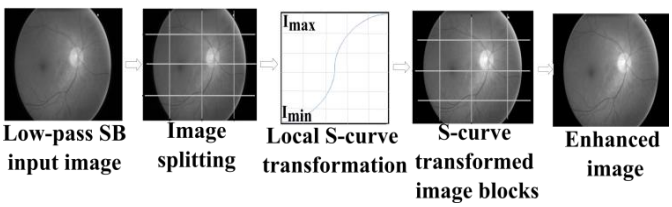

Figure 2. Local S-curve image transformation procedure

This approach utilizes an improved Top-Hat transformation (TH) using the white top-hat (TH_W) and bottom top-hat (TH_B) operations for the low-pass image coefficient mapping. Usage of the same SE leads to poor utilization of pixel neighbor information. To address this, our proposed approach performs TH transformation on multiple scales with varied SE for processing brighter and darker image regions. It defines SE dynamically (D_{se}) based on the *s*-curve optimization principle (illustrated in Figure 2), which transforms larger gray pixel values into small higher ranges and smaller gray pixel values into short-ranges.

Algorithm 1: Retinal image pre-processing
***Input**: Gray scale retinal image: GI*
***Procedure**: PRE-PROCESS(GI)*

1. ***while*** $GI \in DATASET$ ***do***
2. $Mh \leftarrow \alpha_{opt} HIST_{GI} + (1-\alpha_{opt}) HIST_U$
3. $F_{CDF}(I) \leftarrow \sum_{l=0}^{I-1} \left(\frac{Mh}{\sum_{l=0}^{I-1} Mh(l)} \right), I \in GI$ ***from*** 0 ***to*** $I_{\max}$
4. $CDF_T \leftarrow (1+\delta) F_{CDF} - \delta (F_{CDF})^2$
5. ***Generate :*** $I_{AGC} \leftarrow (I_{max}-1) \left(\frac{I}{I_{max}} \right)^{1-CDF_T(I)}$
6. ***Restoration :*** $IMG_{pre} \leftarrow \vartheta (I_{AGC}) + (1-\vartheta)(I_{ORG})$
7. $MG_{PRE} = \bigcup i_{k-1} + (i_k - i_{k-1}) CDF_{pre-k}[I_i]$
   $0 < \vartheta < 1,\ 0 < k < 1$

end
***Output**: Brightness and contrast improved image: IMG_{PRE}*

We have constructed the $D_{SE} = \{SE_1, SE_2 \ldots SE_l\}$ using the initial SE_0 (*A2:S23*). The i^{th} SE is dynamically constructed by operating on SE_0 for *t*-times, and its value is determined by using local *S*-transformation. In the initial iteration, SE_i is obtained with *t=1*. It is followed by low-pass (LS) SB image enhancement (LS_{en}) (*A2:S24*). Local *s*-transformation is operated on LS_{en}. The edge content [38] of the s-curve transformed images (ED_{C_LS}) is measured (*A2:S27*). The distance ($Diff_{max}$) to the original image's edge content value (ED_C) is the deciding factor for *t* value and SE_i (*A2:S28 to S29*). At the end of iterations, the *t* value is determined for D_{se}. Using D_{se} in TH_{W_i} and TH_{B_i}, the LS image is enhanced (LS_{final}) by upgrading brighter (DTH_W) and darker (DTH_B) regions (UBD) at equal rates using the control limit (*K*) based on the edge detection principle (*A2:S9 to S11*).

3.2.2 High-pass coefficient enhancement

The process starts by applying CT to retinal images high-pass (HS) image's DT-CWT coefficients to eliminate noise components. The noise-free HS image ($HS_{Noise\text{-}free}$) is generated using noise variance ($Noise_{SB}$), SB's variance ($Variance_{SB}$) of size $p \times q$ w.r.t. $A \times A$ sized neighborhood area (*A2:S15 to S17*).

3.2.3 Formation of enhanced retinal image

Inverse DT-CWT is applied to combine the processed DT-CWT LS and HS to produce a fully improved retinal image (IMG_{enh}) (*A2:S17*). The process corrects the over-brightness and contrast in the enhanced retinal images, and the significant retinal structures are visually highlighted. The sample results of image preprocessing and enhancement are shown in Figure 3.

3.3 Retinal image feature extraction

The overall feature extraction process is described in the *Algorithm: A3*. Both statistical and graph-based retinal image

features have been extracted.

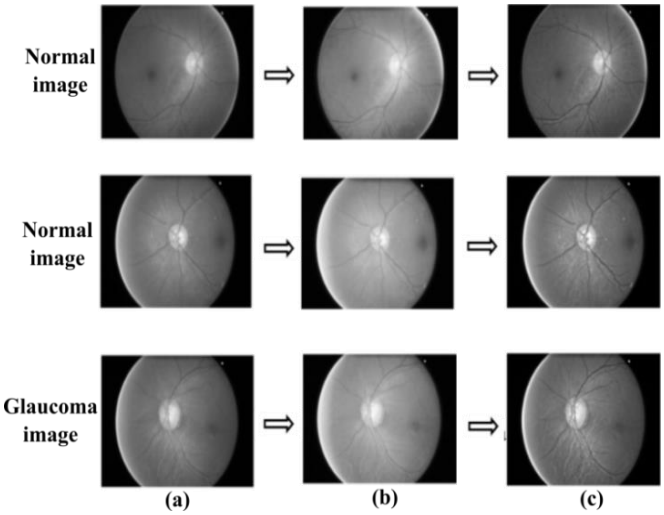

Figure 3. Sample results (a) Original images; (b) Preprocessed images; (c) Enhanced images

3.3.1 Retinal images' statistical features extraction

A two-stage DWT using biorthogonal 6.8 wavelet filter banks has been applied to the enhanced retinal image [39]. The resultant coefficients (*Cf*) are used to extract first- and second-order statistical (FOS and SOS) features. Retinal images' characteristics that fall into the non-stationary and non-linear categories are captured with higher order cumulants (HOC) features using moments of higher order. Since a retinal image comes under the non-stationary signal category, third-order cumulants in various directions (i.e., 10°, 50°, 90°, 130°, and 180°) are considered. Signal amplitude and phase information are used for higher order statistical (HOS) feature extraction in various directions [40].

3.3.2 Retinal images' graph-based features extraction

Graph representations of images provide a structure for pictorial data encoding. The formed graph reflects the image's hidden patterns through its structures, which are highly significant in image description and identification. In this approach, LGS and shortest path (SP) statistics have been considered for graph-based feature extraction.

Algorithm 2: Retinal image enhancement

Input: *Brightness and contrast improved image:*IMG_{PRE}

Procedure*: ENHANCEMENT (*IMG_{enh}*)*

1. ***while*** $IMG \leftarrow IMG_{PRE}$ ***do***
2. $\{LS_{set}, HS_{set}\} \leftarrow DTCWT(IMG)$
3. ***for*** $LS \in \{LS_{set}\}$ ***do***
4. $D_{se} \leftarrow$ *call* D_{se} *construction*
5. $TH_{W_i}(m,n) = LS(m,n) - LS \circ D_{se_i}(m,n)$
6. $TH_{B_i}(m,n) = LS \bullet D_{se_i}(m,n) - LS(m,n)$
7. $DTH_{w_i}(m,n) = TH_{W_{i+1}}(m,n) - TH_{W_i}(m,n)$
8. $DTH_{B_i}(m,n) = TH_{B_{i+1}}(m,n) - TH_{B_i}(m,n)$
9. $UBD = \max_{1 \le i \le l}((\{TH_{W_i}(m,n)\} + \{DTH_{W_i}(m,n)\})$
10. $-(\{TH_{B_i}(m,n)\} + \{DTH_{B_i}(m,n)\}))$
11. $LS_{final} = LS + 1 - \kappa_i(UBD)$
12. ***end***
13. ***for*** $HS \in \{HS_{set}\}$ ***do***
14. $SB \leftarrow CT(HS)$ $p,q : SB\,size$
15. $HS_{Noise-free} \leftarrow \frac{1}{p \times q} \sum_{r,s=1}^{r=p,s=q} \left(\sum_{r,s=1}^{r=p,s=q} (SB_{val}) \right)$ $\frac{\text{Median}(|C_{SB}|)}{\beta}$, $\text{SB}_{\text{val}} = \frac{1}{A^2} \sum_{a_1,a_2=1}^{A} |SB(a_1,a_2)|^2$
16. ***end***
17. $IMG_{enh} \leftarrow \text{DTCWT}_{Inv}(\text{LS}_{\text{final}}, \text{HS}_{\text{Noise-free}})$
18. ***end***

end procedure

Procedure : $D_{se} CONSTRUCTION(IMG_{PRE})$

19. ***for*** $\{LS\} \leftarrow DTCWT(IMG_{PRE})$ ***do***
20. $t \leftarrow 1$
21. ***for*** $LS \in \{LS\}$ ***do***
22. ***while***(TRUE) ***do***
23. $SE_i \leftarrow SE_0 \oplus ... \oplus SE_0$ ***for*** t *times*
24. $LS_{en} \leftarrow LS + [LS(m,n) - LS \circ SE_i(m,n)] -$
25. $[LS \bullet \text{SE}_i(\text{m,n}) - LS(\text{m,n})]$
26. $G_{LS_{en}} \leftarrow C + \frac{R}{1 + \exp\left(\frac{pi - \delta_1}{\delta_2}\right)}$, $pi \in LS_{en}$
27. $ED_{C\_LS} \leftarrow \frac{1}{M * N} \sum_{m=1}^{M} \sum_{n=1}^{N} |G_{LS_{en}}(m,n)|$
28. ***if*** $\left(|ED_C - ED_{C\_LS}| \le Diff_{\max}\right)$ $t \leftarrow t+1$
29. ***else*** *return* $D_{se} \leftarrow SE_i$ ***end if***
30. ***end***
31. ***end***
32. ***end***

Output: *Structurally improved image:* IMG_{enh}

Local graph structure (LGS) features. The LGS feature extraction operates on a graph theory that considers image pixels as vertices ($Vertex_G$) and their neighborhood relations. It applies the threshold operation to neighboring pixels, based on current pixels in different directions. To avoid the imbalanced neighbor covering limitation with the asymmetric LGS, in this approach, a symmetrically shaped neighborhood is considered for every pixel point. The enhanced retinal image pixel gray intensities are considered as vertices. In the earlier work, only the left and right regions of the pixel are considered for forming a symmetric region [41] that represents the pixel's neighbor relationship. In this approach, the top and bottom regions are considered along with the left and right regions to form symmetric regions for every pixel. Symmetric regions are considered for the immediate neighbors of the current pixel in a predefined order, as indicated in Figure 4.

The LGS operator compares pair-wise pixel gray values starting from the center pixel in the given directions. While moving between a pair of points (directions are shown by arrows), the connecting edge is assigned a label of zero in the case of a higher to lower intensity value; otherwise, it is assigned a label of one. This process is continued for every pair of vertices in the central pixel neighborhood symmetric region (SNR). It results in two patterns of size *P* bits: $Pattern_{LR}$

by threshold bits from the left to right regions and $Pattern_{TB}$ by threshold bits from the top to bottom regions. The magnitude of the neighbor relation pattern (NRP) is generated from the threshold operation (*Thr*) (*A3:S6 to S9*).

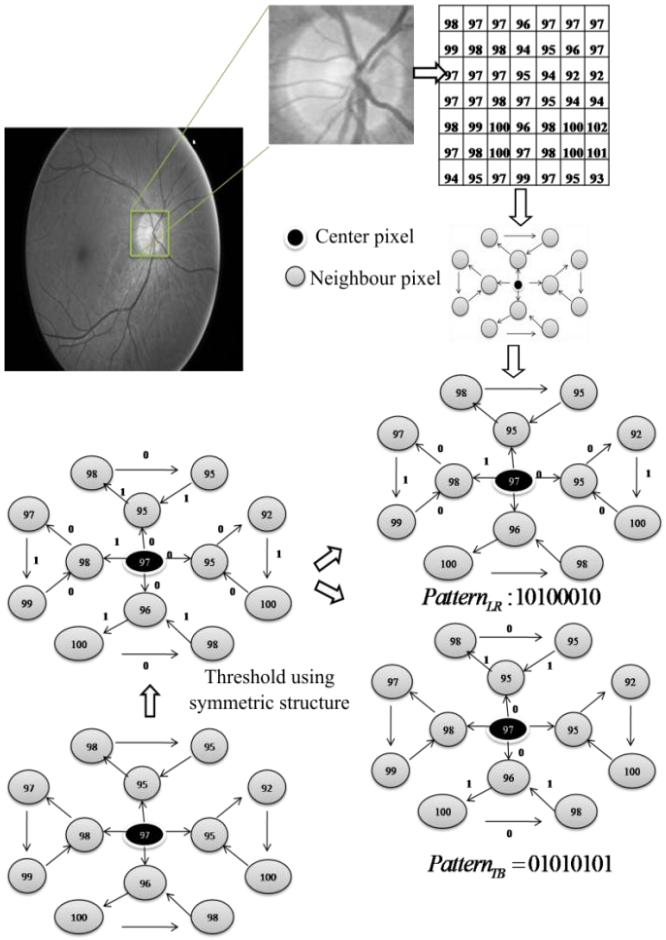

Figure 4. Neighbor relation pattern extraction using LGS operation

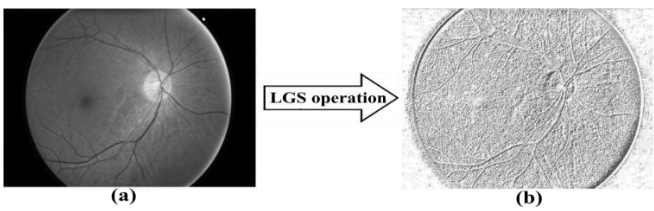

Figure 5. Sample result of proposed LGS (a) Enhanced and (b) Resulted LGS retinal image

A threshold operation is applied on every central vertex (C_V) with horizontal and vertical neighbor vertices (HN_V or VN_V) that results in two magnitude values for the left-to-right (NRP_{LR}) and top-to-bottom directions (NRP_{TB}) of the C_V to generate the final NRP (NRP_{Final}) (*A3:S10*). Each C_V is then replaced with the corresponding NRP_{Final} value to generate mapped retinal images, as shown in Figure 5. A histogram (H_{LGS}) is generated for the resultant retinal LGS image of size $N_r \times N_c$. The histogram features for every intensity level (L) are generated using the probability density ($Prob_{LGS}$) of H_{LGS} (*A3:S12*).

Graph shortest path (GSP) features. The proposed GSP approach is a powerful tool that explores retinal image textures using shortest path statistics between different pixel points in terms of a graph *G (V, E)*. Pixels are represented by vertices $v \in V$ and the relationships between pixel points using edges $e \in E$. The weights of each edge represent the significance of the vertex-pair relationship. Initially, the 2D gray retinal image is converted into 1D data that represents the vertices V in the resultant retinal image graph. Following this, an undirected edge (e) is inserted between pairs of vertices $v_1, v_2 \in V$ based on their Chebyshev distance to form an edge set, $Edge_G$ (*A3:S19*).

The edge weight (E_w) is a combination of the cost of moving from v_1 to v_2 and the transition altitude in the SP finding. To capture the local and global texture patterns of the retinal image, it has been split into multiple equal-sized (N_B) blocks. This makes it possible to analyze and capture the retinal image texture more locally by forming SP-based texture descriptors. The whole retinal image is split into blocks (I_B) and corresponding graphs are generated. The SPs are generated between the source (S_v) and destination (D_v) vertex pairs using Dijkstra's algorithm (*A3:S26*).

To capture the in-depth image texture characteristics, four pairs of vertices are selected to represent the horizontal direction (*0°*), the vertical direction (*90°*), and both diagonal directions (*45°* and *135°*) to find the SPs, as shown in Figure 6. Each image block produces four paths, P_0, P_{90}, P_{45}, and P_{135} for four directions, including all the intermediate vertices for path construction. Then each SP vertices are mapped into corresponding gray level intensities. Thus, each path P_i is now a collection of pixel intensities that appear in its construction. The corresponding mean ($P_{i\text{-}mean}$) is calculated for each path P_i, $i \in \{0°, 45°, 90°, 135°\}$.

As the original retinal image is divided into N_B blocks, every block generates its corresponding $Pi_{\text{-}mean}$. Using these, vectors (Mean_{0^0},Mean_{45^0},Mean_{90^0},Mean_{135^0}) of size N_B are formed by grouping the $Pi_{\text{-}mean}$ corresponding to each direction, as illustrated in Figure 7. Using each Mean_{i^0}, the statistical measures kurtosis, skewness, standard deviation, and quantiles (*Q25, Q50, Q75, Q135*) are generated. By comparing quantiles of one data set with quantiles of another data set, they can be grouped into similar or dissimilar categories [42].

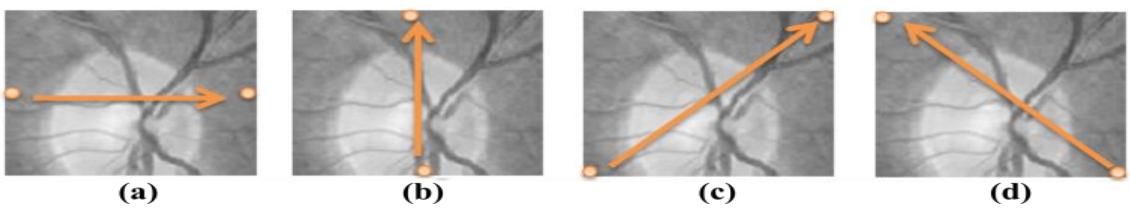

Figure 6. Four directional paths for retinal image (a) Horizontal path (0°), (b) Vertical path (90°), (c) Diagonal path (45°), and (d) Diagonal path (135°)

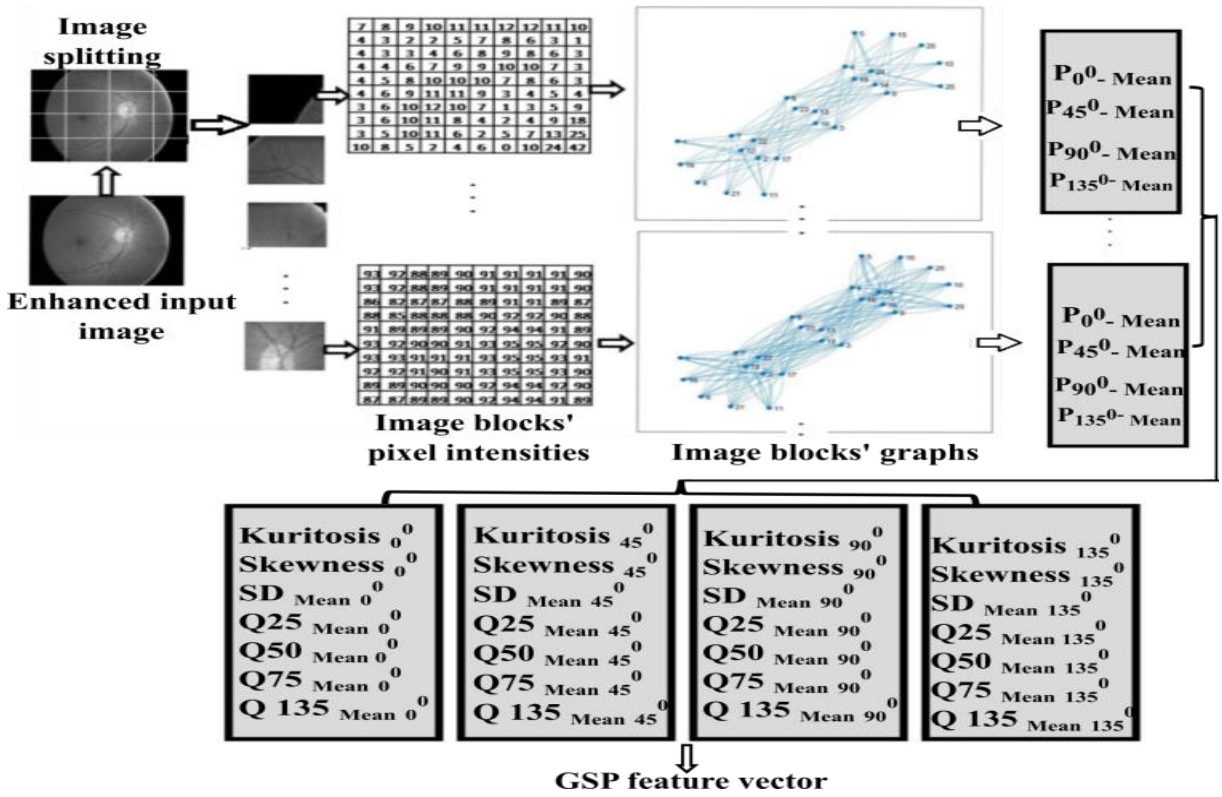

Figure 7. Graph based shortest path retinal image feature extraction

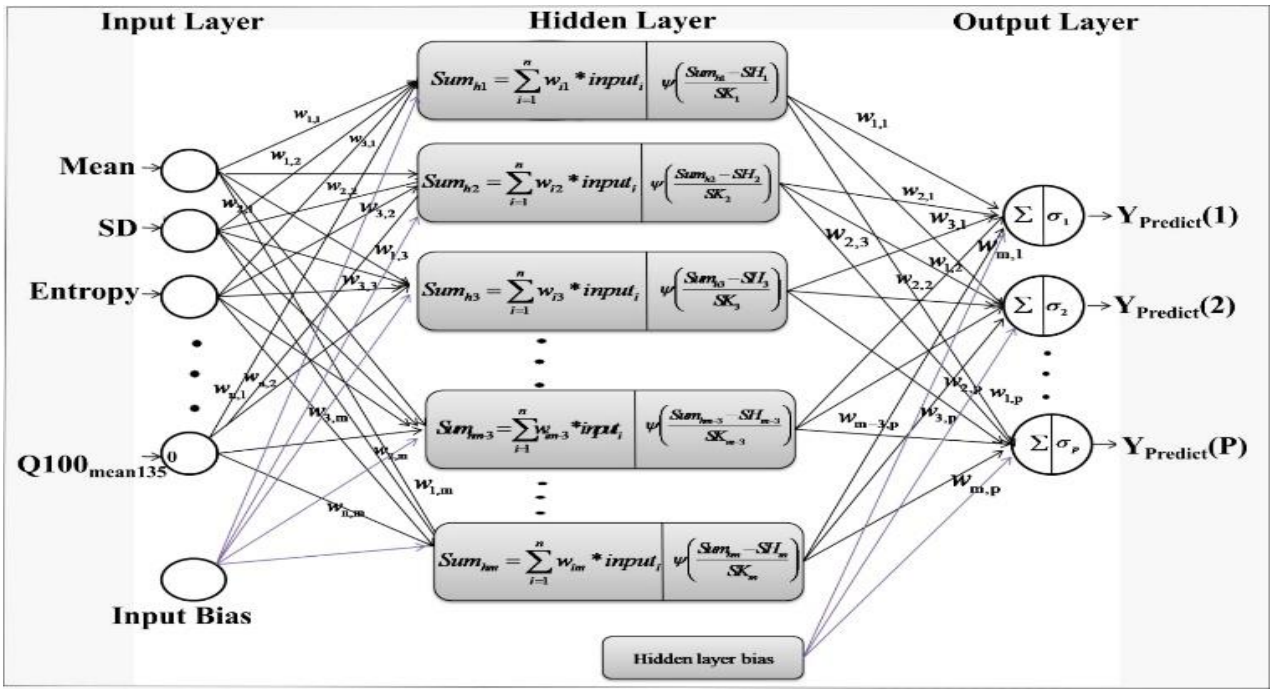

Figure 8. The architecture of WNN

Retinal image classification for glaucoma. WNN and MLP are utilized for glaucoma classification in this approach. The working principles of biological neurons are inherited by NN. The advanced version of NN is WNN. The WNN incorporates both discrete wavelets and MLP learning capabilities to become a powerful classifier. In WNN, instead of non-linear activation functions (such as sigmoid), discrete wavelet functions are used for neuron activation as illustrated in Figure 8. The characterization of input is done using the inner product of weighted input vectors and wavelet base activation functions. To construct the activation function of a neuron, the mother wavelet needed to be selected first. As we have various mother wavelet functions, but some of them have no specific functional representation, their derivatives are difficult to generate. Hence, in our approach, we have considered the mother wavelets such as Mexican hat, Gaussian, Shannon, Morlet, Haar, GGW, and Meyer [43, 44] to construct the activation function for WNN. The supplied retinal features contain significant information about eye abnormalities that should be captured by neurons in the form of activation

functions. In the activation function, the wavelet coefficients recognize the supplied input significance and activate to get the output in the training process.

As shown in Figure 8, the input vector $\{x_1, x_2, \ldots, x_n\}$ represents the retinal image features and the output vector $\{y_1, y_2, \ldots, y_p\}$ represents the p possible outputs predicted by WNN. Each hidden layer is connected to all nodes of the input layer, and receives inputs with a weighting factor w_{ik}. At the hidden layer, the output is generated using wavelet activation functions $\psi_{h_k}(t)$ as:

$$h(k) = \psi_{h_k}(t)\left[\frac{\sum_{i=1}^{n} w_{ik}x_i - SH_k}{ST_k}\right], k = 1,2,\ldots,m \qquad (1)$$

where, SH_k is the shifting factor, ST_k is the scaling factor, and m is the number of hidden layer nodes. The mother wavelet activation function $\psi_{h_k}(t)$ can be one from the mentioned wavelets that yields the least prediction error. The output layer predicts the label by considering weighted inputs from the hidden layer as,

$$y(j) = \sum_{k=1}^{m} w_{kj}h(k), j = 1,2,...,\mathrm{p} \qquad (2)$$

where, w_{kj} is the connection weight. The weights w_{ik} , w_{kj} of input, hidden and output layers are updated iteratively until the objective function attains the lowest possible error value. During this updating process, the values of shifting, scaling, and weights are reached to their optimum values for proper predictions.

On other side, the learning in MLP is based on a back propagation function applied to a feed-forward network. The general structure of MLP includes one input, one output, and one or more hidden layers. In our experiment, the sigmoid activation function is applied for the identification of glaucomatous retinal images. The quantitative and qualitative result analysis is presented in the next section.

Algorithm 3: Retinal image feature extraction
Input: Enhanced retinal images
Procedure: FEATURE EXTRACTION (IMG_{enh})

1. ***for*** $IMG \in IMG_{enh}$ ***do***
2. $Cf \leftarrow DWT_{Level-2}(IMG)$
3. $FoS_{IMG} \leftarrow \{FoS(Cf)\};\ SoS_{IMG} \leftarrow \{GLCM(Cf)\}$
4. $HoC_{IMG} \leftarrow HOC_{A^0}(Cf), A \in \{10,50,90,130,180\}$
5. $HoS_{IMG} \leftarrow Entropy_{HoS}(Cf), Mean_{HoS}(Cf), Ent_{dg}(Cf),$
6. $\{Vertex_G\} \leftarrow Graph\_Mapping(IMG)$
7. ***for*** $V \in \{Vertex_G\}$ ***do***
8. $\{HN_V, VN_V\} \leftarrow SNR(C_V) \Leftarrow C_V \leftarrow V$
9. $NRP_{dr} \leftarrow \sum_{p=0}^{P-1} Thr(C_V, \mathrm{HN}_V)2^p, dr \in \{LR, TB\}$
10. $NRP_{Final} \leftarrow \sqrt{(NRP_{LR})^2 + (NRP_{TB})^2}$
11. $IMG_{LGS} \leftarrow Graph\_Mapping(IMG(V) \Leftarrow NRP_{Final})$
12. $LGS_{IMG} \leftarrow \begin{Bmatrix} Mean(IMG_{LGS}), Variance(IMG_{LGS}), \\ Skewness(IMG_{LGS}), Kurtosis(IMG_{LGS}) \\ Energy(IMG_{LGS}), Entropy(IMG_{LGS}) \end{Bmatrix}$
13. ***end***
14. $\{IMG_{Block}\} \leftarrow Partition(IMG)$
15. ***for*** $\mathrm{IB}^i \in \{IMG_{Block}\}$ ***do***, $i \leftarrow 1 to n$
16. $\{Vertex_G\} \leftarrow Graph\_Mapping(\mathrm{IB}^i)$
17. ***for*** $\mathrm{v}_i, \mathrm{v}_j \in \{Vertex_G\}$ ***do***
18. $e_{ij} \leftarrow (v_i, v_j) \in A_M \left|\max(|x_i - x_j|, |y_i - y_j|) == T_e\right|$
19. $\{Edge_G\} \leftarrow e_{ij}$
20. ***end***
21. ***for*** $e_{ij} \in \{Edge_G\}$ ***do***
22. $e_w \leftarrow \left| I_{vi}(x_i, y_i) - I_{vj}(x_j, y_j) + \frac{I_{vi}(x_i, y_i) + I_{vj}(x_j, y_j)}{2} \right|$
23. $\{E_w\} \leftarrow e_w$
24. ***end***
25. *Identify* $S_v, D_v \in \mathrm{I}_B$ ***for*** $Path_A, A \in \{0^0, 45^0, 90^0, 135^0\}$
26. $\{P_A\} \leftarrow$ ***Dijkstra's procedure*** (S_v, D_v, I_B)
27. $\{P_{A\_mean}\} \leftarrow mean\{P_A\},$
28. $\mathrm{IB}^i_{A\_mean} \leftarrow \{P_{A\_mean}\}, \mathrm{i} \le n$
29. ***end***
30. ***for*** i ***from*** 1 ***to*** n ***do***
31. $\{Mean_A\} \leftarrow mean\{\mathrm{IB}^i_{A\_mean}\}$
32. ***end***
33. $GSP_{IMG} \leftarrow \{Mean_A\}$
34. $Feature\_vector_{IMG} = \begin{Bmatrix} FoS_{IMG}, SoS_{IMG}, HoS_{IMG}, \\ HoC_{IMG}, LGS_{IMG}, GSP_{IMG} \end{Bmatrix}$
35. ***end***
36. ***end***

Output: Retinal images' statistical and graph-based features

4. RESULT ANALYSIS

This approach started with retinal image preprocessing, followed by the enhancement phase. Novel features are extracted from qualitative retinal images, which are fed to MLP and WNN classifiers, and the obtained results are discussed in this section.

Image preprocessing concentrates on improving the image's brightness and contrast. Image brightness is improved using quantile-based histogram modification based on QRTM-based CDF transformation. The results of this approach are compared with those of the HE approaches. The HE over-enhances the image brightness, which leads to unwanted image structural alterations. Improvements in brightness and contrast of the retinal image using the proposed approach and the HE approach are qualitatively compared in Figure 9.

Simultaneously, this method improves the brightness of the image while preserving the contrast difference between retinal structures. In the case of the HE method, both the OD and optic cup (OC) areas are filled with the same contrast, and it becomes difficult to identify the borders of the cup and disc areas, as visualized in Figure 10. The next phase of our approach is the enhancement of preprocessed retinal images to improve the edges of retinal structures.

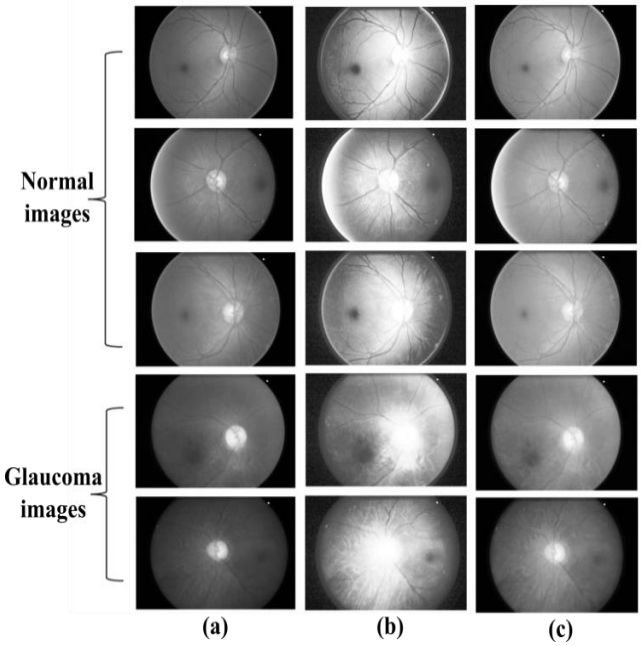

Figure 9. Image pre-processing comparison: (a) input images; (b) Images by HE; (c) Images by the proposed enhancement

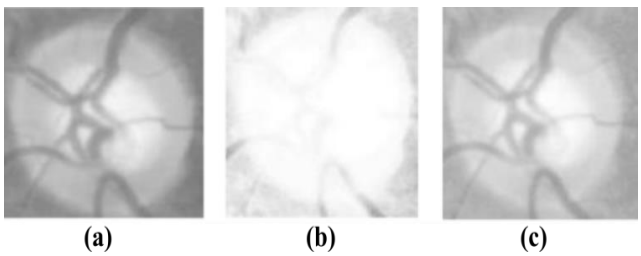

Figure 10. The OD and OC areas of (a) Original image; (b) HE enhanced image; (c) The proposed pre-processing

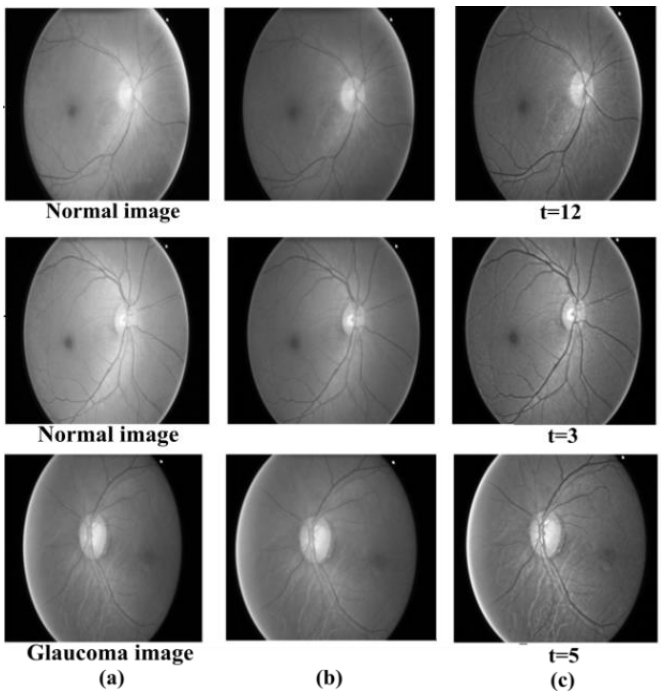

Figure 11. Illustration of D_{SE} usage: (a) pre-processed image; (b) enhanced image with t=0 and (c) enhanced image with different t values of D_{SE} in the proposed method

The enhancement approach is based on independent modifications of low and high sub-band image DT-CWT coefficients using D_{SE}. The value of t is dynamically changed with each image based on the s-curve transformation. In this approach, some images' enhancement stops at smaller values of t, and some images require larger t values, as shown in Figure 11.

Increasing the t value above the value defined by the s-curve transformation has not shown any improvement in the retinal structures. We have employed the mean squared error (MSE) as a quality evaluation metric, and its lower value indicates the originality between the improved and the original images. The MSE is calculated on images resulting from the proposed method and compared with the HE, CLAHE, and RRIE [45] approaches as shown in Table 1.

The comparison results show that enhanced images resulting from the proposed preprocessing and enhancement approach have lower MSE values than other methods in the literature. The MSE histogram plot for RRIE and the proposed enhancement in Figure 12 show that the proposed approach keeps the images closer to the ground truth. For better visibility of the plot, HE and CLAHE results are not included in the plot.

Table 1. Comparison of MSEs of the proposed approach with the other approaches

Sl. No	Image Name	MSE by HE	MSE by CLAHE	MSE by RRIE	MSE by Proposed Approach
1	Im0010	0.0676	0.0114	0.0020	0.0007
2	Im0012	0.0533	0.0084	0.0020	0.0007
3	Im0023	0.0449	0.0110	0.0007	0.0013
4	Im0026	0.0521	0.0081	0.0011	0.0003
5	Im0028	0.0382	0.0092	0.0014	0.0005
6	Im0145	0.0722	0.0134	0.0012	0.0004
7	Im0146	0.0345	0.0114	0.0010	0.0004
8	Im0206	0.1004	0.0216	0.0007	0.0003
9	Im0208	0.0664	0.0117	0.0010	0.0005
10	Im0618	0.1221	0.0195	0.0005	0.0002
11	Im0600	0.0738	0.0131	0.0020	0.0007
12	Im0586	0.0379	0.0131	0.0009	0.0004
13	Im0579	0.0586	0.0093	0.0011	0.0002
14	Im0510	0.0513	0.0116	0.0014	0.0007
15	Im0494	0.0740	0.0123	0.0008	0.0002

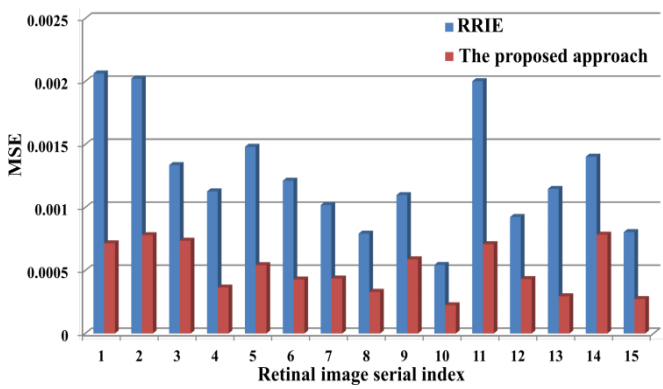

Figure 12. The MSE histogram plots

The enhanced retinal images are utilized to extract statistical and graph-based retinal image features to form a feature vector (FV). The input feature vector set is divided using 70:30 ratio for training and testing/validation. The classification has been carried out by changing the number of nodes in the hidden

layer to find the optimum number. We have conducted several tests to fix the network regulation parameters, i.e., hidden units (HU), batch size (BS), and number of epochs, to get optimum performance. In this approach, the WNN's performance is measured in terms of the testing error rate. In the training processes of WNN and MLP, the network parameters are updated using batch-wise validation and training sets. As shown in Table 2, the wavelet activation function is selected based on the testing error rate of the WNN for 50 epochs. The WNN with Mexican hat wavelet activation function performs best with given retinal image features as it achieves lower testing error.

Table 2. Testing error for various mother wavelet functions

S.No	Wavelet Function	Testing Error
1	Mexican	3.6721%
2	Mayer	9.4129%
3	Gaussian	9.1360%
4	GGW [44]	10.2434%
5	Morlet	9.9666%

Table 3. The performance comparison of WNN and MLP

HU	BS	Epochs	WNN		MLP	
			Verror (%)	Terror (%)	Verror (%)	Terror (%)
		10	7.7577	9.5761	11.7367	16.1169
		50	7.7235	8.5823	11.9211	13.2096
05	128	100	7.7235	8.5823	11.8456	13.1794
		150	7.7235	8.5821	11.7848	13.1992
		200	7.7235	8.5821	11.7059	13.1597
		10	**3.3829**	**5.7433**	13.6408	22.3587
		50	**3.2350**	**3.6721**	11.6332	13.3025
10	64	100	**3.2350**	**3.6551**	11.4426	12.9429
		150	**3.2350**	**3.6550**	11.3670	12.8472
		200	**3.2350**	**3.6550**	11.3458	12.8151
		10	8.2755	14.147	15.3465	28.2071
		50	7.4569	8.8066	10.9941	14.2841
15	32	100	7.4549	8.5861	10.8401	12.6525
		150	7.4549	8.5797	10.8175	12.6018
		200	7.4549	8.5795	10.7969	12.6636
		10	9.1212	17.039	**9.7857**	**16.0400**
		50	7.4751	9.5205	**8.3456**	**9.5431**
25	16	100	7.4482	8.7373	**8.2088**	**9.2851**
		150	7.4479	8.6547	**8.1546**	**9.2164**
		200	7.4479	8.6547	**8.1394**	**9.1934**

In this approach, WNN performance is measured in terms of testing error (*Terror*) and validation error (*Verror*). We have obtained *Terror* as 3.65% for 200 epochs. We have also implemented the MLP network for glaucoma classification and obtained a 9.19% test error for 200 epochs. In this experiment, it has been observed that WNN performance is superior to MLP for the glaucoma classification. The sigmoid activation function is used in MLP with 25 hidden neurons. However, WNN achieved a lower testing error with 10 hidden neurons using the Mexican hat wavelet activation function. In-depth WNN and MLP performance comparisons are shown in Table 3. The WNN achieves minimal testing error at the 50^{th} epoch, irrespective of the number of hidden nodes. Thus, the rest of the experiment has been carried out using the optimal combination, i.e., 10 HU and 64 BS for WNN and 25 HU and 16 BS for MLP.

Initially, the proposed approach has been tested only with statistical features and the classification results are shown in Table 4. Then the proposed approach is tested by considering graph-based features. The classification performance has improved over the statistical features, as shown in Table 5. Finally, the proposed glaucoma screening approach has been tested with both statistical and graph-based retinal image features. The classification performance has tremendously improved, as shown in Table 6. In the case of statistical features, the maximum accuracies achieved with WNN and MLP are 76.4% and 73.1% before enhancement, respectively. The accuracies have been improved to 80.6% and 76.8% after the enhancement. The classification accuracies of WNN and MLP are positively improved with the graph-based retinal image features. Using graph-based features, the maximum accuracies of WNN and MLP are 88.2% and 86.7%, respectively. In this case, the performances of WNN and MLP are improved by an average of 4% with the proposed image enhancement. This case has shown the significance of graph-based features over statistical features. Finally, the combination of both statistical and graph-based features has been tested for the classification using both the WNN and MLP. The accuracy, sensitivity, and specificity plots have been shown in Figure 13.

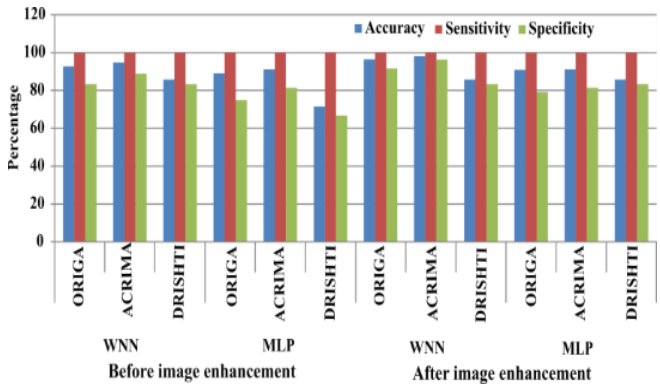

Figure 13. WNN and MLP classification performance plots

This combination has considered the statistical intensity relationships among pixels as well as pixel neighborhood relationship patterns in the identification of glaucomatous images. The WNN has achieved 96.36% and 98.24% accuracy with the ORIGA and ACRIMA datasets, which are far better than the accuracies achieved by MLP, i.e., 90.90% and 91.22%. However, both WNN and MLP have achieved less accuracy, i.e., 85.71% with the DRISHTI, due to its smaller dataset size. Before retinal image enhancement, WNN classifies the images of ORIGA and ACRIMA with accuracies of 92.72% and 94.73%, whereas MLP classifies them with accuracies of 89.09% and 91.22%. The performance of WNN is the same with the DRISHTI dataset with or without enhancement, but the MLP performance is degraded in the absence of image enhancement. The false positive and negative prediction rates are higher with the statistical features when compared with the graph-based features. But these false prediction rates have been minimized in the best possible way with the combination of statistical and graph-based features.

The ROC curves corresponding to statistical features-based, graph-based, and combined features-based glaucoma screening have been depicted in Figures 14-16 for both before and after image enhancement (BE and AE). The glaucoma screening by MLP and WNN using statistical features is suboptimal, as evidenced by the ROC plots in Figure 14, which show a maximum Area Under the Curve (AUC) of 80%. The model is misclassifying images and struggling to capture

relevant patterns with the usage of only statistical features. For graph-based features, both MLP's and WNN's screening performance has relatively improved, with the maximum AUC reaching 89%, as indicated in Figure 15. The screening capacities for MLP and WNN improved considerably with the combination of statistical and graph-based retinal features as shown in Figure 16. However, WNN achieved a maximum AUC of 99%, while MLP's performance reached up to 92% AUC. This indicates that WNN outperforms MLP.

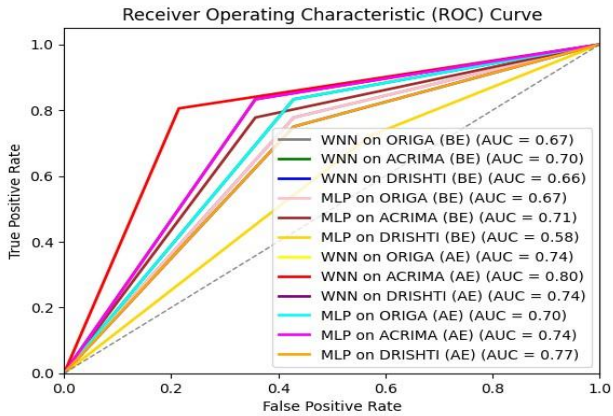

Figure 14. The ROC plot for glaucoma classification using statistical features

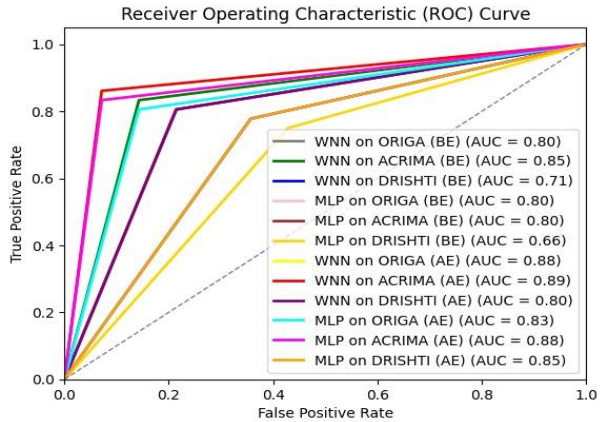

Figure 15. The ROC plot for glaucoma classification using graph features

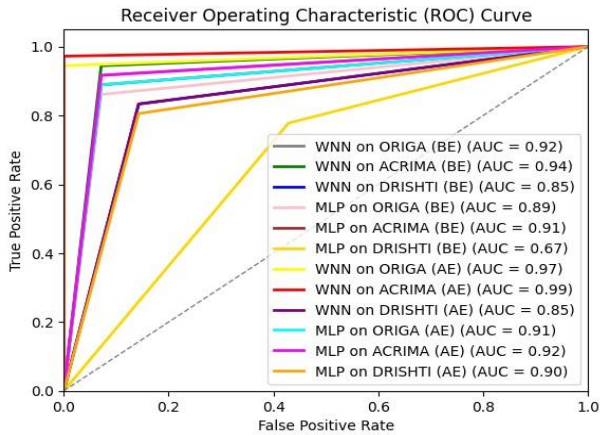

Figure 16. The ROC plot for glaucoma classification using statistical and graph-based features

The accuracy, sensitivity, and specificity plots for various combinations are shown in Figures 17-19. The accuracy has been improved with the application of WNN. The sensitivity of MLP and WNN is almost linear, with or without enhancement. The specificity of both MLP and WNN has been improved with the proposed enhancement. However, the WNN plots are more consistent and optimal than the MLP classification plots.

The performance of the proposed approach has been analyzed with state-of-the-art approaches, as shown in Table 7. Retinal images' texture features are extracted in current approaches [46, 47] using GLCM and run length matrices. These features are utlized by SVM and k-NN for glaucoma screening. However, pre-processing, which includes blood vessel segmentation and removal, might overlook critical structural changes relevant to glaucoma. Additionally, GLCM's sensitivity to image quality factors like resolution and lighting conditions can compromise feature extraction and model generalization. The combination of first-, second-, or higher-order texture features of retinal images is classified using k-NN, NB and SVM [48]. In this approach also blood vessels are removed in the pre-processing phase which has less impact on the classification accuracy. Though the optimized NN are utilized in the study [49], the obtained screening accuracies are quite low since the approach is solely depends only on the lower and higher order texture features. This approach employed a NN with a single hidden layer, whereas the proposed approach utilized WNN, which offer more reliable performance compared to standard NNs. Entropy-based approach [50] is not optimal for glaucoma classification due to their sensitivity to noise and variability in image acquisition. However, this approach did not incorporate any noise reduction or texture improvement techniques during the pre-processing phase, resulting in suboptimal outcomes. Glaucoma screening proves to be more optimal with LBP features compared to first and second order features [51]. By observing these existing approaches, the classification accuracies are improved when the statistical features are considered in combination with other feature categories, such as LBP. It has further been observed that texture enhancement enhances classifier discriminative power and robustness by emphasizing crucial patterns. Thus, in the proposed approach, the combination of statistical features and graph-based features has been considered along with the image specific texture improvement. The obtained results substantiate the significance of this integrated approach, showcasing its effectiveness.

The proposed approach can be applied to screen the other human eye diseases such as diabetic retinopathy, macular edema, vascular occlusions, and retinopathy of prematurity (ROP) from retinal images. The proposed image improvement phase enhances the retinal structures based on specific details within the image. This improves the identification of structural changes associated with different retinal diseases. Furthermore, both statistical and graph-based features have been extracted from the entire area of the fundus image. This feature extraction primarily captures the structural alterations in eye fundus due to retinal diseases. Thus, this approach exhibits high generalizability for screening various retinal diseases.

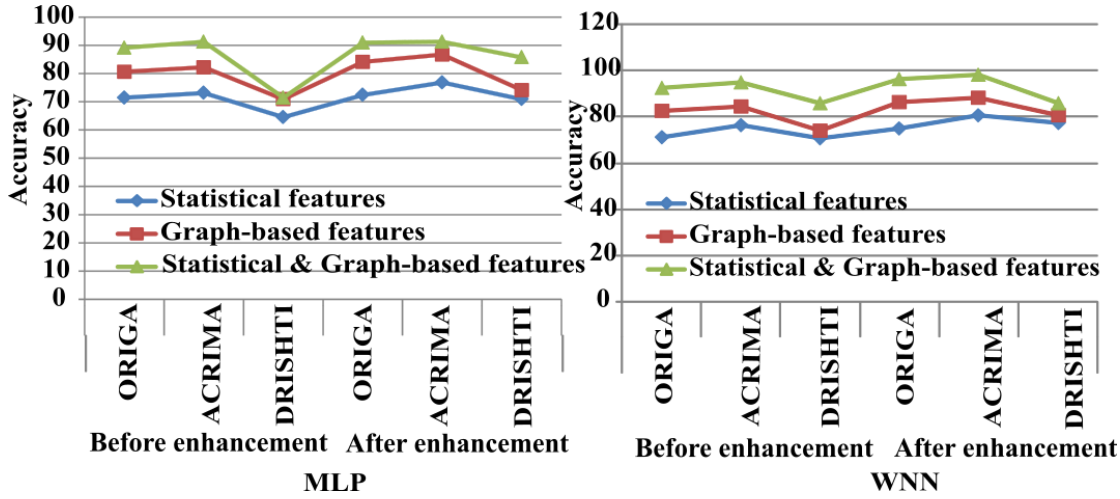

Figure 17. Accuracy plots obtained with MLP and WNN

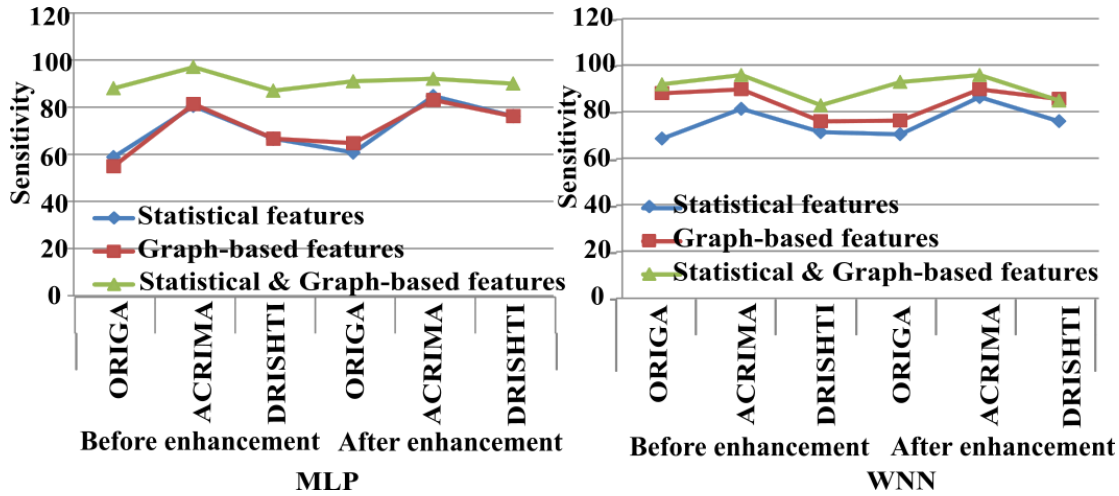

Figure 18. Sensitivity plots obtained with MLP and WNN

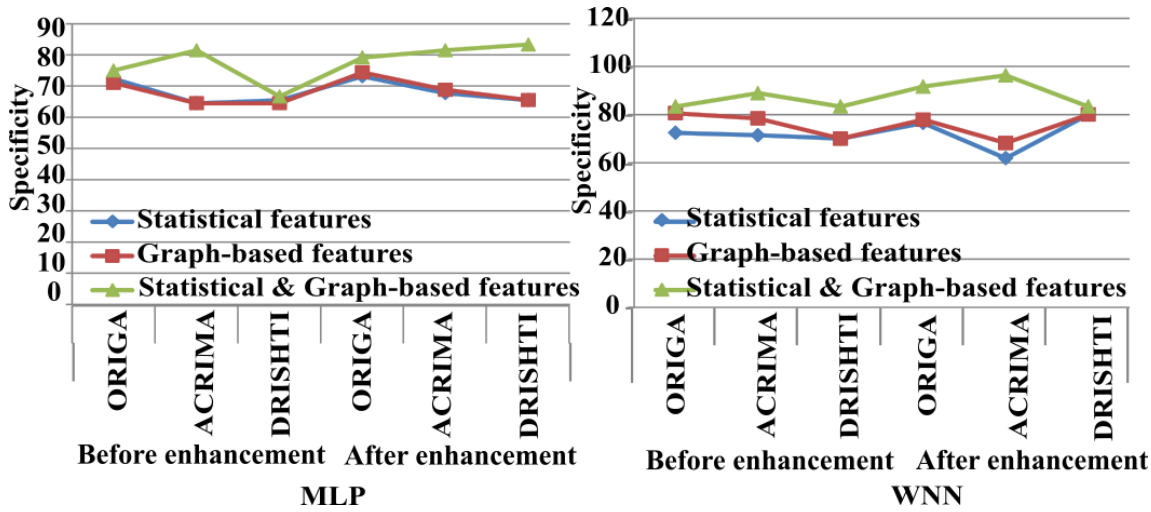

Figure 19. Specificity plots obtained with MLP and WNN

Table 4. The proposed approach's glaucoma classification performance using statistical features

	Dataset	No. of Images	Accuracy (%)	Sensitivity (%)	Specificity (%)	Confusion Matrix (%)			
						T_P	F_P	T_N	F_N
			Before retinal images enhancement						
	ORIGA	650	**71.4**	**68.6**	**72.4**	0.68	0.27	0.73	0.32
WNN	ACRIMA	705	**76.4**	**81.5**	**71.4**	0.81	0.28	0.72	0.19
	DRISHTI	101	**70.9**	**71.4**	**70**	0.71	0.30	0.70	0.29

	ORIGA	650	71.4	58.8	72.4	0.58	0.27	0.73	0.42
MLP	ACRIMA	705	73.1	80.5	64.5	0.80	0.35	0.65	0.20
	DRISHTI	101	64.5	66.6	65.5	0.66	0.34	0.66	0.34
			After retinal images enhancement						
	ORIGA	650	**75**	**70.5**	**76.5**	0.70	0.23	0.76	0.29
WNN	ACRIMA	705	**80.6**	**86.5**	**61.9**	0.86	0.38	0.61	0.13
	DRISHTI	101	**77.4**	**76.1**	**80**	0.76	0.2	0.8	0.23
	ORIGA	650	72.4	60.7	73.1	0.60	0.26	0.73	0.39
MLP	ACRIMA	705	76.8	84.7	67.7	0.84	0.32	0.67	0.15
	DRISHTI	101	70.9	76.1	65.5	0.76	0.34	0.65	0.23

Table 5. The proposed approach's glaucoma classification performance using graph-based features

	Dataset	**No. of Images**	**Accuracy (%)**	**Sensitivity (%)**	**Specificity (%)**	**Confusion Matrix (%)**			
						T_P	**F_P**	**T_N**	**F_N**
			Before retinal images enhancement						
	ORIGA	650	**82.6**	**88.2**	**80.6**	0.88	0.19	0.80	0.11
WNN	ACRIMA	705	**84.4**	**89.9**	**78.4**	0.89	0.21	0.78	0.10
	DRISHTI	101	**74.1**	**76.1**	**70**	0.76	0.3	0.7	0.23
	ORIGA	650	80.6	54.9	71	0.54	0.28	0.71	0.45
MLP	ACRIMA	705	82.2	81.3	64.5	0.81	0.35	0.64	0.18
	DRISHTI	101	70.9	66.6	64.5	0.66	0.35	0.64	0.33
			After retinal images enhancement						
	ORIGA	650	**86.2**	**76.4**	**77.9**	0.76	0.22	0.77	0.23
WNN	ACRIMA	705	**88.2**	**89.9**	**68.2**	0.89	0.31	0.68	0.10
	DRISHTI	101	**80.6**	**85.7**	**80**	0.85	0.2	0.8	0.14
	ORIGA	650	84.1	64.7	74.4	0.64	0.25	0.74	0.35
MLP	ACRIMA	705	86.7	83	68.8	0.83	0.31	0.68	0.16
	DRISHTI	101	74.1	76.1	65.5	0.76	0.34	0.65	0.23

Table 6. The proposed approach's glaucoma classification performance using statistical and graph-based features

	Dataset	**No. of Images**	**Accuracy (%)**	**Sensitivity (%)**	**Specificity (%)**	**Confusion Matrix (%)**			
						T_P	**F_P**	**T_N**	**F_N**
	ORIGA	650	**92.72**	**92**	**83.33**	0.91	0.17	0.83	0.09
WNN	ACRIMA	705	**94.73**	**96**	**88.88**	0.94	0.12	0.88	0.06
	DRISHTI	101	**85.71**	**83**	**83.33**	0.84	0.17	0.83	0.16
	ORIGA	650	89.09	88	75.2	0.86	0.25	0.75	0.14
MLP	ACRIMA	705	91.22	97	81.48	0.95	0.19	0.81	0.05
	DRISHTI	101	71.42	87	66.66	0.87	0.34	0.66	0.13
	ORIGA	650	**96.36**	**93**	**91.66**	0.92	0.09	0.91	0.08
WNN	ACRIMA	705	**99.3**	**96**	**96.29**	0.94	0.04	0.96	0.06
	DRISHTI	101	**85.71**	**85**	**83.33**	0.86	0.17	0.83	0.14
	ORIGA	650	90.9	91	79.16	0.83	0.21	0.79	0.17
MLP	ACRIMA	705	91.22	92	81.48	0.93	0.19	0.81	0.07
	DRISHTI	101	85.71	90	83.33	0.89	0.17	0.83	0.11

Table 7. The performance comparison of the proposed approach with state-of-the-approaches

Reference	**Approach**	**Performance Measures**			**Remarks**
		Accuracy (%)	**Sensitivity (%)**	**Specificity (%)**	
[46]	ML classification using the texture and morphological features	88.3	93.3	83.3	Image preprocessing phase is not applied before feature extraction
[47]	ANN-based classification using statistical features	89.3	98	90	Image pre-processing is not applied
[48]	ML-based classification using FOS, SOS, HOC, HOS features	97.22	91	96	Image enhancement has not been applied before the feature extraction
[49]	Optimized NN-based classification using FOS, SOS, and HOC features	93.1	91.6	94.1	This approach is highly sensitive to false positive or negative predictions
[50]	Entropy features-based classification	91	89	93	Images are not enhanced or purified before feature extraction
[51]	Local binary patterns (LBP) and SOS features	97.5	--	--	Image's quality has not been not improved before pattern extraction
The proposed approach	**WNN-based classification using both statistical and graph-based features**	**99.3**	**96**	**96.29**	**The combination of graph and statistical features from the enhanced images has attained the optimal classification**

5. CONCLUSION

The proposed technique has contributed to all major CAD phases, including retinal image improvement, feature extraction, and classification. Our approach initially concentrated on retinal image quality enhancement, which is carried out in two phases: preprocessing and enhancement. The preprocessing improves the retinal image brightness and contrast using QRTM-transformed CDF-based image quantile histogram modification. The proposed preprocessing method ensures that brightness and contrast are optimized. Image enhancement improves the retinal structures using an independent modification of the retinal images' DT-CWT low and high-pass sub-band coefficients. Retinal image texture patterns are captured using graph-based retinal image features using proposed LGS and GSP paths in various directions, along with statistical features. The glaucoma classification is carried out using WNN and MLP networks by selecting activation functions systematically. In this approach, WNN performs better than MLP for glaucoma classification. The classification results are tabulated for various network parameter combinations. According to the available literature, our strategy is a new approach that combines retinal images' graph-based feature extraction with the WNN-based glaucoma classification. The performance of this approach has been tested with various combinations of statistical and graph-based features. The results obtained have proven the efficacy of the proposed approach.

REFERENCES

[1] Friedman, D.S., O'Colmain, B.J., Munoz, B., Tomany, S.C., McCarty, C., De Jong, P.T.B.M., Nemesure, B., Mitchell, P., Kempen, J., Congdon, N. (2004). Prevalence of age-related macular degeneration in the United States. Arch Ophthalmol, 122(4): 564-572. https://doi:10.1001/archopht.122.4.564

[2] Kolb, H. (2003). How the retina works: Much of the construction of an image takes place in the retina itself through the use of specialized neural circuits. American Scientist, 91(1): 28-35. http://www.jstor.org/stable/27858152

[3] Nath, M.K., Dandapat, S. (2012). Techniques of glaucoma detection from color fundus images: A review. IJ Image, Graphics and Signal Processing, 4(9): 44-51. https://doi: 10.5815/ijigsp.2012.09.07

[4] Kaur, R., Juneja, M., Mandal, A.K. (2019). Computer-aided diagnosis of renal lesions in CT images: A comprehensive survey and future prospects. Computers & Electrical Engineering, 77: 423-434. https://doi.org/10.1016/j.compeleceng.2018.07.024

[5] Gupta, B., Tiwari, M. (2016). Minimum mean brightness error contrast enhancement of color images using adaptive gamma correction with color preserving framework. Optik, 127(4): 1671-1676. https://doi.org/10.1016/j.ijleo.2015.10.068

[6] Kim, Y.T. (1997). Contrast enhancement using brightness preserving bi-histogram equalization. IEEE Transactions on Consumer Electronics, 43(1): 1-8. https://doi.org/10.1109/30.580378

[7] Sim, K.S., Tso, C.P., Tan, Y.Y. (2007). Recursive sub-image histogram equalization applied to gray scale images. Pattern Recognition Letters, 28(10): 1209-1221. https:// doi.org/10.1016/j. patrec.2007.02.003

[8] Wang, C., Peng, J., Ye, Z. (2008). Flattest histogram specification with accurate brightness preservation. IET Image Processing, 2(5): 249-262. https://doi.org/10.1049/iet-ipr:20070198

[9] Arici, T., Dikbas, S., Altunbasak, Y. (2009). A histogram modification framework and its application for image contrast enhancement. IEEE Transactions on image Processing, 18(9): 1921-1935. https://doi.org/10.1109/TIP.2009.2021548

[10] Khare, V. (2023). Automatic detection of exudates in retinal image using statistical techniques. Ingénierie des Systèmes d'Information, 28(1): 255-261. https://doi.org/10.18280/isi.280130

[11] Luo, Z., Jia, Y., He, J. (2019). An optic disc segmentation method based on active contour tracking. Traitement du Signal, 36(3): 265-271. https://doi.org/10.18280/ts.360310

[12] Mallat, S.G. (1989). A theory for multiresolution signal decomposition: The wavelet representation. IEEE Transactions on Pattern Analysis and Machine Intelligence, 11(7): 674-693. https://doi:10.1109/34.192463

[13] Selesnick, I.W., Baraniuk, R.G., Kingsbury, N.C. (2005). The dual-tree complex wavelet transform. IEEE Signal Processing Magazine, 22(6): 123-151. https://doi.org/10.1109/MSP.2005.1550194

[14] Feng, P., Pan, Y., Wei, B., Jin, W., Mi, D. (2007). Enhancing retinal image by the Contourlet transform. Pattern Recognition Letters, 28(4): 516-522. https://doi.org/10.1016/j.patrec.2006.09.007

[15] Sujitha, Subhajini. (2022). Identification and categorization of microaneurysms in optic images by applying DTCWT and log Gabor characteristics. Revue d'Intelligence Artificielle, 36(5): 725-730. https://doi.org/10.18280/ria.360509

[16] Liao, M., Zhao, Y.Q., Wang, X.H., Dai, P.S. (2014). Retinal vessel enhancement based on multi-scale top-hat transformation and histogram fitting stretching. Optics & Laser Technology, 58: 56-62. https://doi.org/10.1016/j.optlastec.2013.10.018

[17] Tabbakh, A., Barpanda, S.S. (2022). Evaluation of machine learning models for plant disease classification using modified GLCM and wavelet based statistical features. Traitement du Signal, 39(6): 1893-1905. https://doi.org/10.18280/ts.390602

[18] Dua, S., Acharya, U.R., Chowriappa, P., Sree, S.V. (2011). Wavelet-based energy features for glaucomatous image classification. IEEE Transactions on Information Technology in Biomedicine, 16(1): 80-87. https://doi.org/10.1109/TITB.2011.2176540

[19] Nirmala, K., Venkateswaran, N., Kumar, C.V. (2017). HoG based naive bayes classifier for glaucoma detection. In TENCON 2017-2017 IEEE Region 10 Conference, Penang, Malaysia, pp. 2331-2336. https://doi.org/10.1109/TENCON.2017.8228250

[20] Zemmal, N., Azizi, N., Sellami, M., Zenakhra, D., Cheriguene, S., Dey, N., Ashour, A.S. (2018). Robust feature selection algorithm based on transductive SVM wrapper and genetic algorithm: Application on computer-aided glaucoma classification. International Journal of Intelligent Systems Technologies and Applications, 17(3): 310-346. https://doi.org/10.1504/IJISTA.2018.094018

[21] Yoshida, T., Iwase, A., Hirasawa, H., Murata, H., Mayama, C., Araie, M., Asaoka, R. (2014). Discriminating between glaucoma and normal eyes using optical coherence tomography and the 'Random Forests' classifier. PloS One, 9(8): e106117. https://doi.org/10.1371/journal.pone.0106117

[22] Shubhangi, D.C., Parveen, N. (2019). A dynamic ROI based glaucoma detection and region estimation technique. International Journal of Computer Science and Mobile Computing, 8(8): 82-86.

[23] Septiarini, A., Khairina, D.M., Kridalaksana, A.H., Hamdani, H. (2018). Automatic glaucoma detection method applying a statistical approach to fundus images. Healthcare Informatics Research, 24(1): 53-60. https://doi.org/10.4258 /hir.2018.24.1.53

[24] de Sousa, J.A., de Paiva, A.C., Sousa de Almeida, J.D., Silva, A.C., Junior, G.B., &Gattass, M. (2017). Texture based on geostatistic for glaucoma diagnosis from fundus eye image. Multimedia Tools and Applications, 76: 19173-19190. https://doi.org/10.1007/s11042-017-4608-y

[25] Singh, A., Dutta, M.K., ParthaSarathi, M., Uher, V., &Burget, R. (2016). Image processing based automatic diagnosis of glaucoma using wavelet features of segmented optic disc from fundus image. Computer Methods and Programs in Biomedicine, 124: 108-120. https://doi.org/10.1016/j.cmpb.2015.10.010

[26] Fraz, M.M., Remagnino, P., Hoppe, A., Uyyanonvara, B., Rudnicka, A.R., Owen, C.G., Barman, S.A. (2012). Blood vessel segmentation methodologies in retinal images-a survey. Computer Methods and Programs in Biomedicine, 108(1): 407-433. https://doi.org/10.1016/j.cmpb.2012.03.009

[27] Salam, A.A., Khalil, T., Akram, M.U., Jameel, A., Basit, I. (2016). Automated detection of glaucoma using structural and non-structural features. Springerplus, 5: 1-21. https://doi.org/10.1186/s40064-016-3175-4

[28] Noronha, K.P., Acharya, U.R., Nayak, K.P., Martis, R.J., Bhandary, S.V. (2014). Automated classification of glaucoma stages using higher order cumulant features. Biomedical Signal Processing and Control, 10: 174-183. https:// doi.org/ 10.1016/ j.bspc.2013.11.006

[29] Acharya, U.R., Dua, S., Du, X., Chua, C.K. (2011). Automated diagnosis of glaucoma using texture and higher order spectra features. IEEE Transactions on Information Technology in Biomedicine, 15(3): 449-455. https:/doi.org/10.1109/TITB.2011.2119322

[30] Abusham, E.E., Bashir, H.K. (2011). Face recognition using local graph structure (LGS). In Human-Computer Interaction. Interaction Techniques and Environments: 14th International Conference, HCI International 2011, Orlando, FL, USA, July 9-14, 2011, Proceedings, Part II. Springer Berlin Heidelberg, 14: 169-175. https://doi.org/10.1007/978-3-642-21605-3_19

[31] Junior, J.J.D.M.S., Backes, A.R., Cortez, P.C. (2013). Texture analysis and classification using shortest paths in graphs. Pattern Recognition Letters, 34(11): 1314-1319. https://doi.org/10.1016/j.patrec.2013.04.013

[32] Li, H.A., Du, Z.M., Zhang, J., Li, Z. (2019). A retrieval method of medical 3D models based on sparse representation. Journal of Medical Imaging and Health Informatics, 9(9): 1988-1992. https://doi.org/10.1166/jmihi.2019.2831

[33] Naidana, K.S., Barpanda, S.S. (2023). A unique discrete wavelet & deterministic walk-based glaucoma classification approach using image-specific enhanced retinal images. Computer Systems Science & Engineering, 47(1). https://doi.org/10.32604/csse.2023.036744

[34] Shaw, W.T., Buckley, I.R. (2009). The alchemy of probability distributions: Beyond Gram-Charlier expansions, and a skew-kurtotic-normal distribution from a rank transmutation map. arXiv Preprint arXiv: 0901.0434. https://doi.org/10.48550/arXiv.0901.0434

[35] Huang, S.C., Cheng, F.C., Chiu, Y.S. (2012). Efficient contrast enhancement using adaptive gamma correction with weighting distribution. IEEE Transactions on Image Processing, 22(3): 1032-1041. https://doi.org/10.1109/TIP.2012.2226047

[36] Kingsbury, N.G. (1998). The dual-tree complex wavelet transform: A new technique for shift invariance and directional filters. In IEEE Digital Signal Processing Workshop. Citeseer, 86: 120-131.

[37] Selesnick, I.W., Baraniuk, R.G., Kingsbury, N.C. (2005). The dual-tree complex wavelets transform. IEEE Signal Processing Magazine, 22(6): 123-151. https://doi.org/10.1109/MSP.2005.1550194

[38] Gupta, S., Porwal, R. (2016). Appropriate contrast enhancement measures for brain and breast cancer images. International Journal of Biomedical Imaging, 2016(1): 4710842. https://doi.org/10.1155/2016/4710842

[39] Santosh, N.K., Barpanda, S.S. (2022). Wavelet and PCA-based glaucoma classification through novel methodological enhanced retinal images. Machine Vision and Applications, 33(1): 11. https://doi.org/10.1007/s00138-021-01263-w

[40] Chua, K.C., Chandran, V., Acharya, U.R., Lim, C.M. (2010). Application of higher order statistics/spectra in biomedical signals-A review. Medical Engineering & Physics, 32(7): 679-689. https://doi.org/10.1016/j.medengphy. 2010. 04. 009

[41] Abdullah, M.F.A., Sayeed, M.S., Muthu, K.S., Bashier, H.K., Azman, A., Ibrahim, S.Z. (2014). Face recognition with symmetric local graph structure (SLGS). Expert Systems with Applications, 41(14): 6131-6137. https://doi.org/10.1016/j.eswa.2014.04.006

[42] Wilcox, R.R., Erceg-Hurn, D.M. (2012). Comparing two dependent groups via quantiles. Journal of Applied Statistics, 39(12): 2655-2664. https://doi.org/10.1080/02664763. 2012.724665

[43] Grossmann, A., Morlet, J. (1984). Decomposition of Hardy functions into square integrable wavelets of constant shape. SIAM Journal on Mathematical Analysis, 15(4): 723-736. https://doi.org/10.1137/0515056

[44] Wang, G., Guo, L., Duan, H. (2013). Wavelet neural network using multiple wavelet functions in target threat assessment. The Scientific World Journal, 2013(1): 632437. https://doi.org/10.1155/2013/632437

[45] Li, D., Zhang, L., Sun, C., Yin, T., Liu, C., Yang, J. (2019). Robust retinal image enhancement via dual-tree complex wavelet transform and morphology-based method. IEEE Access, 7: 47303-47316. https://doi.org/10.1109/ACCESS.2019.2909788

[46] Muthmainah, M.U., Nugroho, H.A., Winduratna, B. (2019). Glaucoma classification based on texture and morphological features. In 2019 5th International Conference on Science and Technology (ICST),

Yogyakarta, Indonesia, pp. 1-6. https://doi.org/10.1109/ICST47872.2019.9166325
[47] Rahouma, K.H., Mohamed, M.M., Hameed, N.S.A. (2019). Glaucoma detection and classification based on image processing and artificial neural networks. Egyptian Computer Science Journal, 43(3).
[48] Thakur, N., Juneja, M. (2020). Classification of glaucoma using hybrid features with machine learning approaches. Biomedical Signal Processing and Control, 62: 102137. https://doi.org/10.1016/j.bspc.2020.102137
[49] Jerith, G.G., Kumar, P.N. (2020). Recognition of Glaucoma by means of gray wolf optimized neural network. Multimedia Tools and Applications, 79(15): 10341-10361. https://doi.org/10.1007/s11042-019-7224-1
[50] Rebinth, A., Kumar, S.M., Kumanan, T., Varaprasad, G. (2021). Glaucoma image classification using entropy feature and maximum likelihood classifier. Journal of Physics: Conference Series, 1964(4): 042075. https://doi.org/10.1088/1742-6596/1964/4/042075
[51] Latha, G., Priya, P.A. (2022). Glaucoma retinal image detection and classification using machine learning algorithms. Journal of Physics: Conference Series, 2335(1): 012025. https://doi.org/10.1088/1742-6596/2335/1/012025

NOMENCLATURE

I	Gray scale intensity
m,n	Coefficients' row and column positions
R	Rows
C	Columns
M,N	Total rows and columns
Cf	DWT coefficients
t	Count in the SE formation
e	Graph edge

Greek symbols

α, ϑ	Constants between 0 to 1
δ	
K	Control limit
β	Median adjustment factor

Subscripts

i,j	Vertex position
C	Edge content
G	Graph
A^0	Angle
dr	Direction
V	Graph vertex
w	Weight
B	Image block number
se	Struturing element
min, max	Minimum and maximum intensitites
LR	Left-to-right
TB	Top-to-bottom